Nuclear Instruments and Methods in Physics Research A 336 (1993) 310–321
North-Holland

NUCLEAR INSTRUMENTS & METHODS IN PHYSICS RESEARCH Section A

UHE cosmic ray event reconstruction by the electromagnetic detector of EAS-TOP

M. Aglietta [b,c], B. Alessandro [c], P. Antonioli [a,c], F. Arneodo [a,c], L. Bergamasco [a,c], A. Campos Fauth [d], C. Castagnoli [b,c], A. Castellina [b,c], C. Cattadori [e], A. Chiavassa [a,c], G. Cini [a,c], B. D'Ettorre Piazzoli [f], G. Di Sciascio [f], W. Fulgione [b,c], P. Galeotti [a,c], P.L. Ghia [b,c], M. Iacovacci [f], G. Mannocchi [b,c], C. Morello [b,c], G. Navarra [a,c], L. Riccati [c], O. Saavedra [a,c], G.C. Trinchero [b,c], P. Vallania [b,c] and S. Vernetto [b,c]

[a] *Istituto di Fisica dell'Università, Torino, Italy*
[b] *Istituto di Cosmo-Geofisica del CNR, Torino, Italy*
[c] *Istituto Nazionale di Fisica Nucleare, Torino, Italy*
[d] *Instituto di Fisica, Universidade Estadual de Campinas, Campinas, Brazil*
[e] *Istituto Nazionale di Fisica Nucleare, Milano, Italy*
[f] *Dipartimento di Scienze Fisiche dell'Università di Napoli and INFN, Napoli, Italy*

Received 2 June 1993

UHE cosmic rays are studied by means of the detectors of the different components of secondaries produced by their interactions in the atmosphere (EAS).

We describe and discuss the reconstruction techniques and accuracies of the e.m. detector of EAS-TOP. They allow, besides independent high resolution measurements of UHE γ-ray astronomy, good correlation possibilities with the detectors of the different EAS components

1. Introduction

Cosmic rays at high energies ($E_0 > 10^{14}$ eV) have to be studied by means of the extensive air shower (EAS) technique, i.e. by detecting the secondaries produced in the atmosphere by the interactions of the primary particles.

Recent arrays incorporate detectors of the different components of EAS (electromagnetic, muonic, hadronic, atmospheric Cherenkov light) and are structured to measure the energy content and the geometry of each of them, in order to provide a reconstruction of individual events as complete as possible.

Detectors have therefore to combine good accuracies in measurements and reconstruction capabilities with large sensitive areas (in order to have significant measurements at the lowest energies of interest), and large effective collecting areas (to collect a sufficient number of events at the highest energies of operation).

In this context the study of the e.m. component has a fundamental role, due to the large effective areas that can be achieved, the energetic content, and the good relation to the primary energy. Moreover, improving the stability and the resolutions (mostly angular, but also energetic and spatial) of the e.m. detectors is still one of the main tools to increase the sensitivity of the measurements in the field of UHE gamma-ray astronomy.

The EAS-TOP installation at Campo Imperatore [1] (Gran Sasso Laboratories, in central Italy) is a multicomponent detector intended to operate in the fields of VHE–UHE γ-ray astronomy, studies of energy spectra and primary composition, UHE interactions and cosmic-ray anisotropies in the energy range 10^{14}–10^{17} eV.

In the present paper we will describe its e.m. detector, the calibration procedures, and discuss the reconstruction techniques and accuracies (first data on the detector technical characteristics were presented in ref. [2]).

2. The EAS-TOP array

The array is located at Campo Imperatore (2005 m a.s.l., above the underground Gran Sasso Laboratories,

atmospheric depth 810 g/cm^2, 42.5° lat. North, 13.5° long. East). It includes detectors of:

a) the electromagnetic component: 29 modules (in the configuration that we will discuss, 37 in its final one) of scintillator detectors (10 m^2 each) distributed over an area of $\approx 10^5$ m^2. From the sample of the particle densities in the different sites (obtained from amplitude measurements), the core location, the slope of the lateral distribution function and the shower size are obtained. The arrival directions are determined by the times of flight among the different detectors.

b) The GeV muons and > 50 GeV hadrons: a calorimeter of dimensions 12×12 m^2 now in operation (24×12 m^2 in its final configuration), covered by a 15 cm thick lead slab, and consisting of 9 layers of iron absorbers 13 cm thick, interleaved by the sensitive layers. Each of the sensitive layers consists of 3 planes of streamer tubes ($3 \times 3 \times 1200$ cm^3 each tube): two of them operating in streamer mode for muon counting and tracking, and one in "quasi" proportional controlled gain mode for hadron calorimetry [3]. The resolution in the measurement of the muon directions, from the tracking technique, is $\sigma_\theta = 0.9°$ [4].

c) The atmospheric Cherenkov light: eight steerable telescopes (one in operation), each of them supporting four 0.6 m^2 parabolic mirrors, one of which is equipped with an imaging device, with pixels of dimensions 2.5 mm corresponding, with the used optics, to $\Delta\theta = 0.2°$ [5].

d) EAS radio emission: three antennas 15 m high, located on different sides of the array, at distances of 200 m, 400 m and 550 m from each other, operating in two wave bands: 350–500 kHz and 1.8–5 MHz [6].

e) Moreover EAS-TOP operates in coincidence with the detectors located in the underground Gran Sasso Laboratories. The sites are separated by $\Delta h = 1000$ m in altitude (corresponding to ≈ 3000 m w.e., and $E_{\mu\text{th}} = 1.4$ TeV); the relative zenith angle is $\langle\theta\rangle \approx 30°$ [7,8]

3. The electromagnetic detector

3.1. The modules

Each of the 10 m^2 modules is split into 16 individual scintillators (NE102A, 80×80 cm^2 area, 4 cm thick).

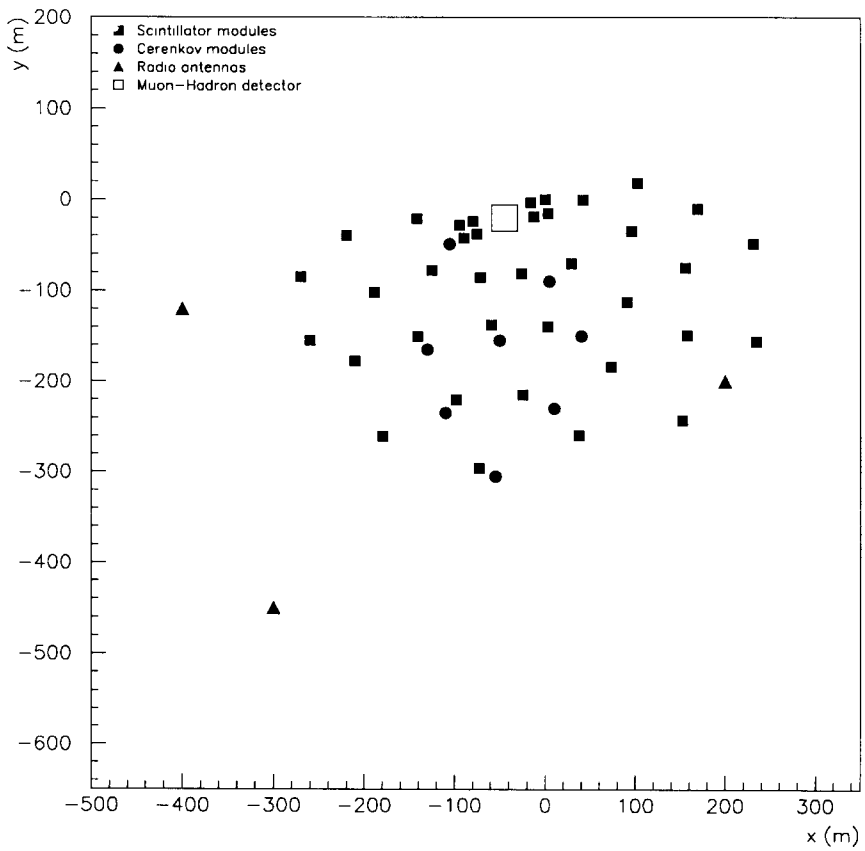

Fig. 1. The EAS-TOP array.

The containers of the scintillators are built by stainless steel boxes (1 mm thick), internally painted with a white diffusing coating (observation is performed in diffusion mode, with photomultipliers located below the scintillator at a distance $d = 30$ cm). Each scintillator is viewed by a photomultiplier XP3462B for timing and particle density measurements from $n_p \approx 0.1$ m^{-2} to 40 m^{-2} (HG pms). The four central scintillators are equipped with an additional similar PM but with a maximum linearity divider, for large particle density measurements ($n_{pmax} \approx 400$ m^{-2}, LG pms).

The electronics inside each module consist of:

a) two mixers of the 16 (and 4 central) PM outputs for further discrimination and amplitude measurements;
b) double threshold discriminators of the quoted signal (0.3 of a minimum ionizing particle for the triggering condition and ≈ 0.1 m.i.p. for timing measurements);
c) a multiplexer and a discriminator for test and calibration runs of the individual PMS;
d) a passive voltage divider, driven in remote, to adjust the HVs of each individual PM;
e) a microprocessor connected through fiber optics to the main computer to handle the quoted operations.

All such equipment is housed in a hut built by 2.7 mm iron (mean thickness) and thermostabilized within ± 3°C in any external condition

3.2. The array

Trigger formation and all measurements are performed in a control room (length of connection cables ≈ 350 m). The trigger is realized by means of Programmable Logic Units CAEN C85; ADCs and TDCs are 11 bit LeCroy 2249W and 2228A respectively.

Except for eight modules organized in two squared configurations near the calorimeter, the array is organized in ten subarrays, that include a central module and five or six modules positioned on circles of radii $r = 50$–80 m, interconnected with each other (see fig. 1). Any fourfold coincidence ($\Delta t = 350$ ns) of the central module of a subarray, together with three consecutive modules on the circle, triggers the data acquisition of the array. Relative measurements of times of flight are performed within the subarrays (which allows a resolution of 0.5 ns with standard electronics); the timing information is extended to the whole array by means of the modules that take part in different subarrays (that further allow multiple measurements of the same delay).

Coincidences between subarrays are performed on a pattern unit ($\Delta t = 2$ μs).

The recording time of the events is provided by a rubidium oscillator (stability $< 10^{-11}$/month), synchronized by the signals provided by the national radio network (the obtained accuracy in the UTC of individual events is ≈ 100 μs)

3.3. Events classification

Events are, in analysis, divided into different classes, the ones concerning this discussion being:

1) S_1 (frequency ≈ 1.5 Hz): at least a whole 6- or 7-fold subarray has triggered and the highest particle density has been recorded by a module not located at the edges of the array ("internal events");

2) S_e (frequency ≈ 20 Hz): events with less than a full subarray fired (4–6 modules), or for which the largest number of particles has been recorded on the border of the array, the core position being therefore expected at the edge or outside the array.

4. Reconstruction of shower size, core location and lateral distribution function

The core location, the lateral distribution function and the shower size (N_e) are determined for "internal events" S_1 from the numbers of particles recorded by each module, that are obtained from the energy losses in the scintillators.

In the following we will discuss the calibration procedure, the reconstruction technique and accuracies. Such accuracies are obtained from simulations that take into account the detectors responses, and are checked by internal consistency of data, and by comparison with the responses of the detectors of other EAS components.

4.1. The detectors and the gain adjustments

With the discussed technique (section 3.1) the photoelectron yield is ≈ 40 pe./m.i.p., and the time resolution, always for a single particle, is $\Delta t < 1.4$ ns.

The amplitude responses of the individual scintillators are adjusted and checked by using the single particle spectra, from the ratio $R = N_1/N_2$ between the number of counts (N_2) above the predetermined channel (CH1) corresponding to the peak of the distribution, and the number of counts (N_1) between the minimum of such distribution (CH0) and CH1 [2]. The relation between the detector's gain G and R is: $\Delta G/G = -0.27\Delta R$. Such calibration and the checking procedures are performed by on-line programs through the chain described in section 3.1.

4.2. The amplitude calibrations

The analysis is performed in units of "equivalent minimum ionizing particles", whose experimental spec-

trum of energy losses is obtained, for HG PMS, by triggering the module in single mode. Thus essentially muons at minimum ionization are detected, crossing the scintillator at a mean angle of 36.9°. Such a spectrum is compared to a simulated one, that takes into account the angular distribution and the Landau fluctuations. The obtained mean energy loss of the detected muons is $\langle \delta E \rangle = 10.3$ MeV.

The mean energy losses of vertical m.i.p. can then be obtained from geometrical considerations: $\langle \delta E_0 \rangle = 8.2$ MeV.

The relation between the ADC counts and the number of detected particles is obtained by recording the single muon spectra, at first with no amplification, and then amplified by fixed and stable factors of 10 and 30.

As the ADC counts relative to HG PMS overflow at about 400 particles/10 m^2, to extend the measurement to higher densities the LG pms are used. Since they cannot be calibrated with the single particle spectra, their calibration is performed through the HG PMS, by correlating the ADC outputs of the two PMS in the overlapping region, and then extrapolating to higher densities (the ADC counts overflow thus at ≈ 4000 particles/10 m^2).

To check the stabilities, ADC pedestals and linearities are continuously monitored during the data taking.

4.3. The reconstruction technique

The reconstructions are performed by means of a χ^2 fit in which the densities recorded by each module are compared with the theoretical NKG lateral distribution function [9]:

$$\rho(r) = c(s)\left(N_e/r_0^2\right)(r/r_0)^{(s-2)}(1 + r/r_0)^{(s-4.5)},$$

with Molière radius $r_0 = 100$ m. In fact such theoretical expression represents a very good fit to the data over a wide energy range; fig. 2 shows the mean experimental lateral distribution, for events with $N_e > 10^5$ and the fit obtained with the NKG expression.

The fitting procedure is divided in various steps (the arrival directions obtained as described in section 5 are used):

a) First, core location (x_c, y_c) is determined, with an algebrical method, as the barycenter of the four modules with the largest particle densities.

b) Then s and N_e are fitted with the core located in fixed positions over a grid, of ± 15 m with step 5 m, centered in the position determined before. The parameters giving the minimum value of χ^2 are chosen as starting values for the final fit.

c) At last, all four parameters (x_c, y_c, s, N_e) are fitted. Even in this step it is advantageous to separate the minimization procedures; so alternatively (x_c, y_c) or (N_e, s) are optimized with the other couple of parameters fixed, in an iteration procedure.

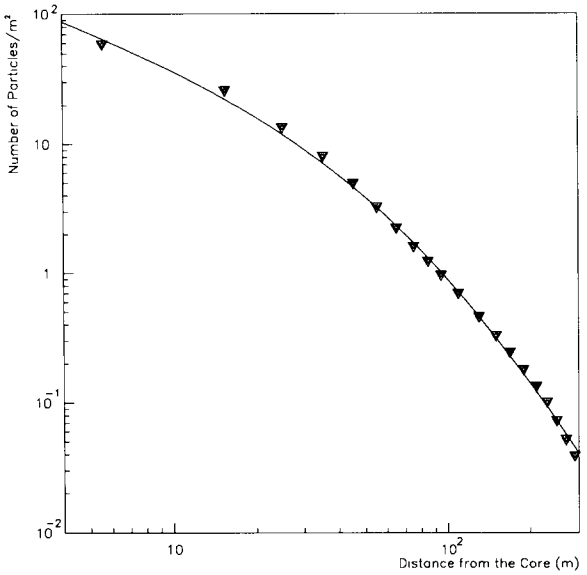

Fig. 2. Mean experimental lateral distribution of EAS, for internal events (S_1) with $N_e > 10^5$. The solid line shows the best fit to the NKG formula ($s = 1.24$).

All minimizations are performed using the CERN library MINUIT [10]. The whole procedure takes a computing time of 0.52 s/100 m.i.p.s. per event.

4.4. Sources of errors in the density measurements

Of major importance in the minimization procedure is the correct knowledge of the experimental errors and fluctuations of the density data. They can be partly measured, and partly calculated; in detail they are due to:

a) The Poisson fluctuations of the number of particles crossing the detector surface, including the "cos θ" reduction of such surface for inclined showers. This contribution (in "m.i.p. approximation", i.e. neglecting the effects of conversion, multiplication, and stopping particles in the scintillator) is:

$$\sigma_n^2 = n \cos\theta$$

b) The fluctuations of the energy losses of individual particles (from single particle spectra):

$$\sigma_n^2 = (0.15)^2 n.$$

c) The variations of the photomultiplier gains with time. This, measured by a continuous monitoring of the gains through the single particle spectra, gives:

$$\sigma_n^2 = (0.035n)^2.$$

d) The fluctuations in the light collections, in ADC linearities, and in PM non-uniformities, measured by

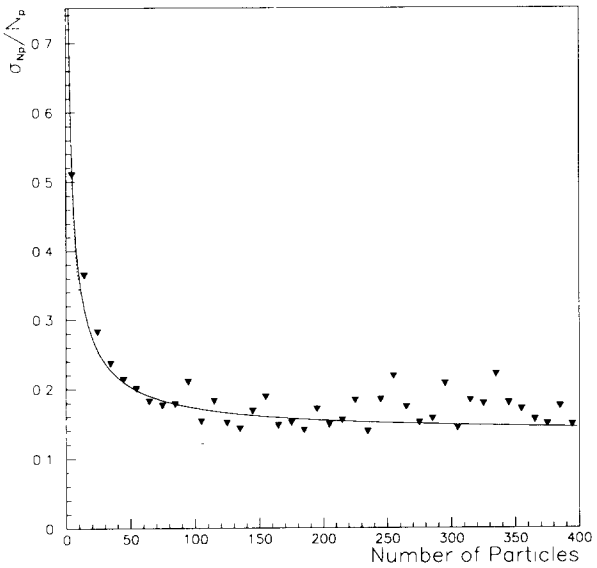

Fig. 3. Fluctations of the particle number detected by a module (N_p) vs N_p. The experimental points are obtained as the rms of the distribution of percent differences in the number of particles measured by two modules that are, within 5 m, at the same core distance (and that are therefore expected to measure the same particle density). The dotted line shows the behaviour of the fluctuations discussed in the text (see section 4.4). In order to compare the obtained formula with the experimental points, we have added to the expected values a term that takes into account the error in the core location: the result is shown by the solid line.

looking at the same scintillator with two photomultipliers calibrated at the same gain. Comparing the two ADC counts, the obtained error as a function of the particle density is:

$$\sigma_n^2 = \frac{n^2}{2}\left(0.076/\sqrt{n} + 0.065\right).$$

e) Concerning the low gain PMS a further term is added, taking into account the fluctuations due to the statistical errors in their calibration procedure from the high gain PMS, giving:

$$\sigma_n^2 = (0.1n)^2.$$

This behaviour of the measurement uncertainties as a function of the particle numbers is checked, with the experimental EAS data, by selecting couples of modules within similar (in our case 5 m) reconstructed distances from the core, and then comparing the recorded densities. The comparison between the experimental and the previously discussed behaviour is shown in fig. 3 (a contribution taking into account the fluctations due to the errors in the reconstruction of the core location is also added).

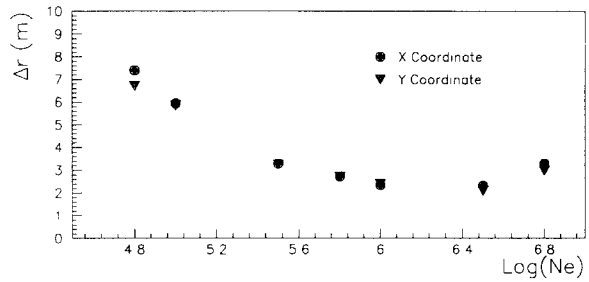

Fig. 4. Resolution in the core location vs the shower size.

4.5. The resolutions

The accuracies in the determination of core location, slope of l.d.f. (s parameter in NKG formalism), and shower size are calculated as a function of N_e by analyzing simulated showers.

For the simulated events the core locations are sampled over an area large enough to cover the whole array, the slopes of lateral distribution function (s) from a Gaussian distribution with mean value $\langle s \rangle = 1.2$, and rms, $\sigma_s = 0.15$ (as found from the analysis of the experimental data), the arrival directions uniformly with zenith angle $0° < \theta < 40°$ and azimuth angles $0° < \phi < 360°$ (the experimental errors on arrival directions are included).

The mean number of particles expected in each detector is calculated through the NKG formula, then fluctuated over the experimental errors described above to obtain the "experimental" data. From such values the trigger condition is obtained, and the reconstruction is performed. The results of the comparison between the input and the reconstructed data are shown in figs. 4–6. For shower sizes $N_e > 2 \times 10^5$, for which the detection efficiency is $\approx 100\%$ (and the effective area, obtained from the same simulation $A_{eff} = 4 \times 10^4$ m^2), we have:

$\sigma_{N_e}/N_e = 0.1$,

$\sigma_{\Delta x_e} = \sigma_{\Delta y_e} = 5$ m,

$\sigma_s = 0.1$.

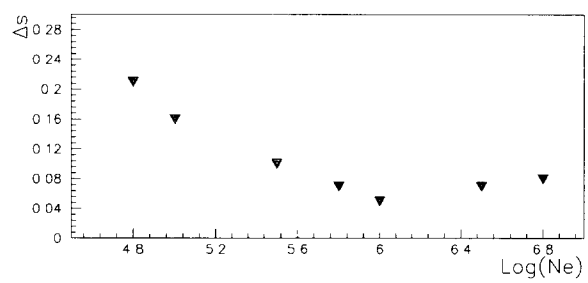

Fig. 5. Resolution in the determination of the slope of the l.d.f. (s) vs the shower size

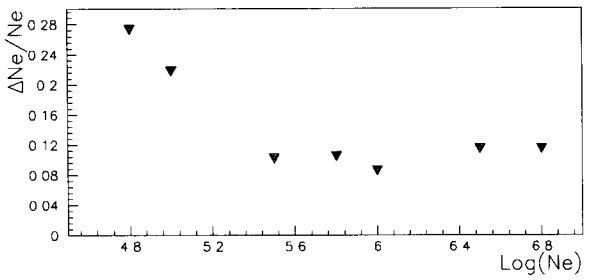

Fig. 6. Percent error in size determination vs the shower size.

An experimental check of the reconstruction accuracies can be obtained from the comparison of the core locations obtained from EAS-TOP and the projections at the surface of the TeV muons recorded by the MACRO detector operating deep underground in the coincidence events [7]. The results obtained in coincidence with the first supermodule of MACRO give (for $N_e > 10^5$ and $N_\mu > 1$):

$\sigma_{\Delta x_c} = 11$ m, $\quad \sigma_{\Delta y_c} = 6$ m,

well compatible with the calculated reconstruction accuracies of both detectors.

4.6. The transition effect

In order to evaluate the detector response to the e.m. component of EAS, a Monte Carlo simulation of the cascade development in the atmosphere and in the apparatus has been carried out using the EGS4 code [11].

The atmosphere has been assumed uniform with the EAS-TOP level density (0.8 atm); the detector has been approximated by an infinite layer of iron (3.7 mm, the mean roof plus box thickness) and an infinite layer of plastic scintillator (4 cm thick). γ primaries ranging from 100 GeV to 1 TeV have been launched from different heights (100–700 g cm^{-2}, corresponding to age parameter $s = 0.5$–1.5) and the secondary particles are followed down to 0.5 MeV K.E. (electrons and positrons) and 50 keV (photons).

The number of $e^{\pm}$ (N_e') at the EAS-TOP (810 g cm^{-2}) level and the energy deposit in the scintillator are then calculated, the latter being converted to an "equivalent number of vertical particles" (N_e) using the mean vertical energy loss $\langle \delta E_0 \rangle = 8.2$ MeV (see section 4.2).

The ratio N_e/N_e' gives the overall contribution to the transition effect, due to γ conversions in the iron and plastic scintillator ($N_\gamma \cong 10 N_e$), stopping particles inside the scintillator, producing of δ-rays. Its value is largely independent from the primary γ-ray energy and s, the dependence from the zenith angle being:

$N_e/N_e' = -0.17 \cos\theta + 1.2$.

This value is hence used to convert the reconstructed value of N_e as obtained in m.i.p. units to the total number of $e^{\pm}$ (N_e').

5. Reconstruction of the arrival direction

EAS arrival directions are obtained from the times of flights among the different modules. In the following we will discuss the sources of errors, and the reconstruction technique and accuracies. These are obtained from internal consistency of data, study of the moon shadowing effect on primary cosmic rays, and comparison with the data from the detectors of other EAS components.

5.1. Sources of indetermination

Different sources of fluctuations (of technical and physical origin) contribute to the indetermination of the arrival directions:

– from the technical point of view: the fluctuations in the light collection and in the transit time in the pms (already quoted: $\Delta t < 1.4$ ns for single particles), the relative adjustements of the signals from the 16 PMs of each module, the TDC calibrations, the uncertainties in the measurement of the absolute time differences between the modules, and the electronics stability;

– from the EAS structure point of view: the disk thickness connected with the effect of particles sampling, the disk curvature and hence the distance from the core.

5.1.1. Technical factors: calibrations and compensations

The uncertainties due to technical factors (PMs, electronics, stability) are minimized by means of calibration and compensation procedures.

5.1.1.1. Adjustment of PM relative timing. The time resolution of a single scintillator detector, for single particles, is $\Delta t < 1.4$ ns (see section 4.1 [2]).

Since each module signal for timing measurements is provided through the analog sum of 16 PMs (operating at different HV and therefore with different transit times) it is necessary that they correctly overlap. This is achieved (after the gain calibrations) by adjusting the time delays between each out of the 16 and a reference one. The obtained precision is $\Delta T_{PM} < 0.5$ ns. Changes of HV supplies, corresponding to changes of gain $\Delta G/G$ up to $\approx 10\%$, do not affect such adjustement.

5.1.1.2. TDC calibrations. The TDC slopes are measured by generating TDC stop pulses through calibrated cable delays. The cable lengths have been measured with 0.1 ns precisions by means of a LeCroy 9400 oscillograph. The maximum deviation of the measured

TDC slopes from the nominal ones (0.5 ns/channel) is $< 5\%$; periodical checks indicate a stability within 0.5 ns over the whole range of time delays.

5.1.1.3. Modules relative timing The relative timing of the modules is calibrated on a six months basis by measuring the delays between the coincident signals from each module and a small reference test counter (based on a 20×20 cm^2 plastic scintillator NE102A, with fixed cable length and PM HV supply) shifted over all of them. This measurement provides the delay $T_0 = T_{\text{module}} - T_{\text{test counter}}$ in the time response of each module to the same particles, with accuracy $\delta T_0 \approx 0.5$ ns, where $T_{\text{test counter}}$ is kept constant for all the detectors during the calibration procedure.

5.1.1.4. Compensations for variations in time, and array stability tests. To compensate for changes of electronics circuits or variations in transit times, the time delays are renormalized on a 12 hours time-base. The mean values of the delays measured by each TDC, $\langle \text{TDC} \rangle_0$, in an acquisition run immediately before or after the T_0 calibrations, is used as the reference one, and the same quantity, $\langle \text{TDC} \rangle$ (precision 0.25 ns), is calculated every 12 hours. Each counter firing time, t_f', is determined by correcting the measured one, t_f, for T_0 and the variations of $\langle \text{TDC} \rangle$ with respect to the calibration one $\langle \text{TDC} \rangle_0$:

$$t_f' = t_f - \langle \text{TDC} \rangle - (T_0 - \langle \text{TDC} \rangle_0),$$

where each term has been converted from TDC counts to time by means of the correct TDC slope.

Arrival directions obtained with sets of T_0 (and therefore of $\langle \text{TDC} \rangle_0$) determined at different epochs are compatible within 0.2°.

5.1.2. The EAS structure

The shower structure affects the measurement of the arrival direction through the disk curvature and its thickness. The former is due to the delay of the shower particles with respect to the plane tangent to the EAS front in the core, and causes an error in the arrival direction measurement which depends on the core distance; the latter represents the dispersion of EAS electrons with respect to such curved front and thus introduces an indetermination because of the sampling effect (depending therefore on N_e and the core distance, due to the different particle densities). Figs. 7a and 7b show the measured mean values of the quoted delays and their fluctuations, respectively, as a function of the core distance, for different numbers of detected particles.

The influence of the discussed disk shape on the reconstruction of the arrival direction has been measured by comparing the arrival angles obtained, for internal events (in the plane approximation), by the subarray including the core, and all other subarrays fired. Fig. 8 shows the behaviour of such differences as a function of the core distance, giving, for our geometry, a systematic error of 0.03°/m.

5.2. The reconstruction technique

To compensate for the quoted physical effects, and limit the computing time, the reconstructions of the arrival directions are performed, for internal events (S_1), by using the timing informations of the 6 (or 5) modules located around the one recording the largest number of particles. In fact, being located in nearly symmetrical positions around the core, they record

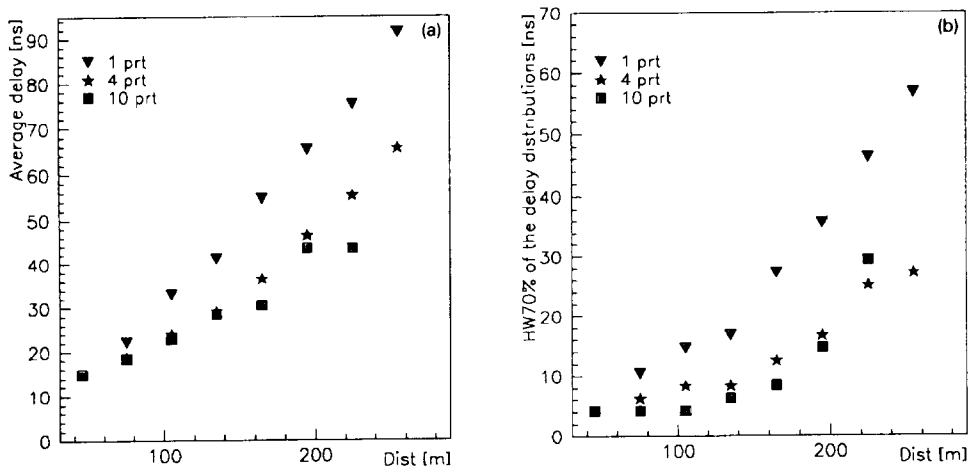

Fig. 7. Mean value (a) and width (b) of the delay distributions with respect to the shower plane front, as a function of the core distance, for different numbers of detected particles.

similar number of electrons at similar core distances, and are therefore affected by nearly equal delays due to the curvature and the sampling effects. This allows the use of a plane approximation for the shower front, without reconstructing the core location and the curvature for each event. A comparison of the results obtained from this procedure, and a full one, taking into account the measured curvature of the shower front, together with the core location, gives differences within 0.1°, thus much smaller than the resolution (see section 5.3). This is since the quoted modules, due to the best timing data and detectors separation ($\approx$ 100 m), provide the most sensitive angular information, and therefore give the main contribution to the value of χ^2 in the fit.

For external or low energy events S_e the arrival directions are again obtained in the plane approximation of the EAS front (since the core is not located, and the curvature effect cannot be taken into account), but averaging over all the triggered subarrays. In this case the error due to the EAS structure is dominant, and is taken into account (section 5.3.1).

5.3. The resolutions

5.3.1. Relative measurement

The first evaluation of the angular resolution is performed through a check of the internal consistence of the data. Each subarray is divided into two sub sets and the two reconstructed shower directions $\psi_{1,2}$ are compared. In order to have two independent measurements this operation is performed on the 7-fold subarrays only, each subsets including thus, besides the central one, three independent detectors, chosen alternatively on the circle (being hence affected in the same way by the EAS curvature and fluctuations). If σ_ψ is the width of the distribution of such differences, $\sigma_\alpha = \sigma_\psi/2$ is the arrival direction error when all the detectors of the subarray are used. The integral distribution of $\Delta\psi$, for showers with zenith angle $\theta < 40°$, is shown in fig. 9, for both S_1 and S_e events, compared with the distributions obtained by assuming Gaussian shapes of fluctuations with different values of s.d. As it can be seen, a single gaussian distribution does not fit the whole of experimental data; 70% of the data are enclosed inside an error box with $\sigma_\psi < 1.8°$ for S_1 events and with $\sigma_\psi < 3.2°$ for S_e events.

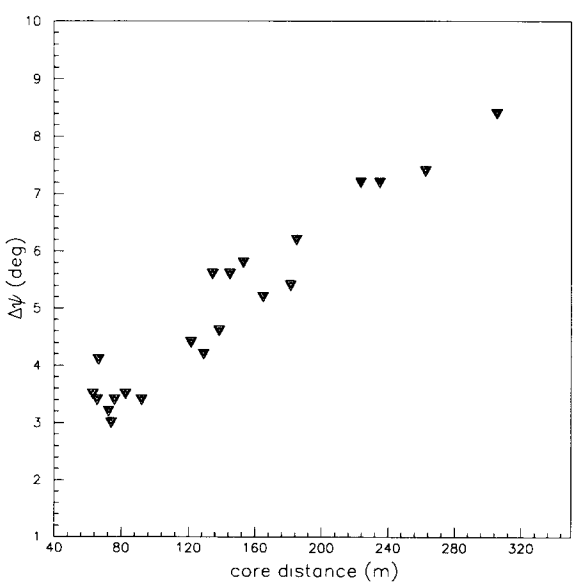

Fig. 8. Systematic errors in the determinations of EAS arrival directions vs subarray core distances.

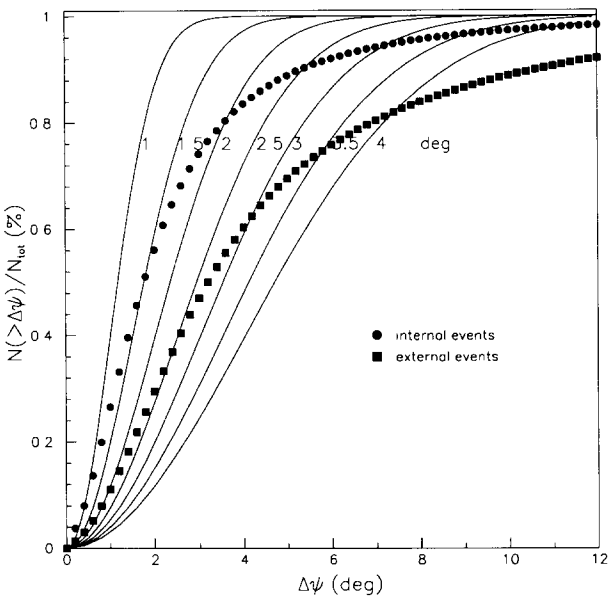

Fig. 9. Integral distributions of the arrival directions differences as obtained from two parts of a subarray (see text) for internal and external events. The expectations from Gaussian distributions with different s.d. values are also shown (full lines).

The errors in the angular reconstruction is then $\sigma_{\alpha 1} \approx 0.9°$ for the former (S_1) and $\approx 1.6°$ for the latter (S_e) events, neglecting any possible systematic error. By adding, for S_e events, the effect of core location shown in fig. 8 for an average core distance $\approx$ 100 m, we obtain $\sigma_{\alpha e} \approx 3.4°$.

For events S_1, the angular resolution has been studied as a function of the number of detected particles and hence of the shower size (N_e). Such dependence is clearly seen in fig. 10 where the integral distributions of the arrival directions differences of $\Delta\psi$ are plotted for different intervals of N_e, and moreover we can see that the errors distribution tend to be Gaussian for large N_e. Fig. 11 shows the behaviour of the angular

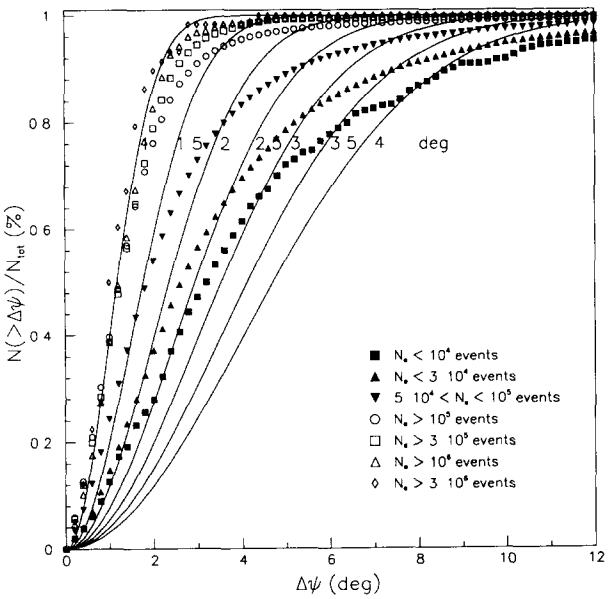

Fig. 10. Integral distributions of the arrival directions differences (see fig. 9) for internal events, for different shower size values.

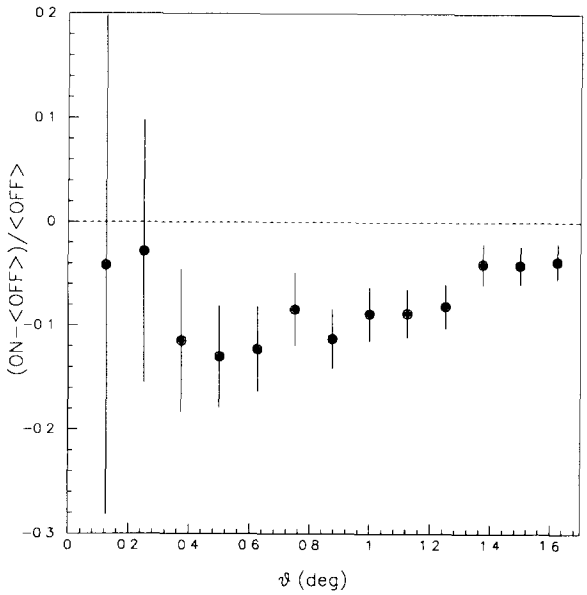

Fig. 12. Integral behaviour of the deficit of events in the Moon direction vs the opening angle from its center.

resolution σ_α vs N_e: as expected, it becomes better as the shower size increases (it is $\approx 0.5°$ for $N_e > 10^5$).

5.3.2. Absolute measurement: the Moon shadowing effect

In the absence of a steady "candle" in the UHE γ-ray sky, the only possible absolute measurement of the angular resolution for an EAS array is the detection of the "shadow" cast by the Moon on the high energy primary cosmic ray flux (a similar effect is due to the Sun, except that the Moon provides a much better statistics at our latitudes) [12]. Since its angular diameter is $\approx 0.52°$, and since it has no magnetic field, such a calibration is possible for the EAS-TOP array which has an angular resolution $< 1°$.

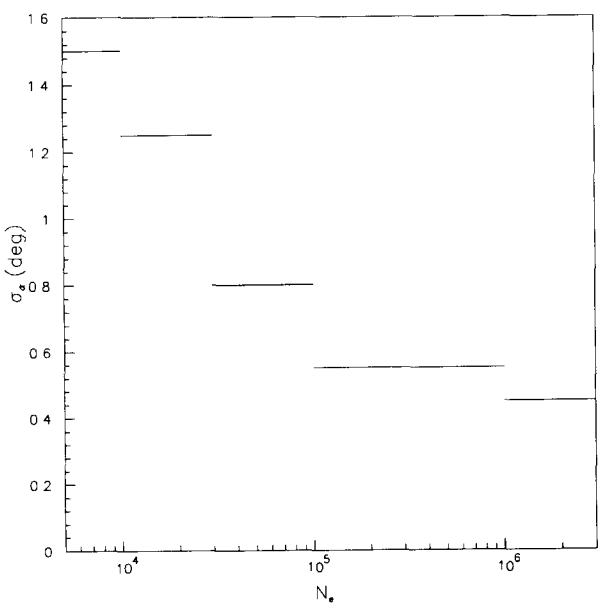

Fig. 11. Internal events angular resolution vs shower size.

The data used in the study of the shadow of the Moon have been collected in 20 months of measurement (March–December 1990, January–December 1992), for a total of ≈ 681 hours. The technique used in the analysis is the ON–OFF one, i.e. three regions of the sky have been considered, one centered on the "source" (ON) and the other two (OFF) at the same declination but shifted in right ascension of $\pm 2\ \Delta\alpha$, with $\Delta\alpha = 1.6°$. Only days of operation in which all the three cells have been observed from their rising to setting (zenithal angle $< 40°$) have been used.

Fig. 12 shows the integral behaviour of the experimental "excess" $(\mathrm{ON} - \langle\mathrm{OFF}\rangle)/\langle\mathrm{OFF}\rangle$ vs the angular distance θ from the centre of the Moon. The observed deficit has a significance of 4 s.d. and, inside 1.6°, it amounts to 179 events (against 4717 of background). If we use the procedure adopted in the case of search for UHE γ-ray sources, given the primary cosmic rays flux, this corresponds to a deficit of 2×10^{-13} events cm^{-2} s^{-1} thus giving an indication of the sensitivity of the EAS-TOP array.

The trend of the deficit vs the angular displacement from the center of the Moon allows an experimental

evaluation of the detector point spread function $F(\theta)$ [12]. This is shown in fig. 13 together with the expected one assuming a Gaussian angular resolution with s.d. 1.0°. The obtained best fit gives $\sigma_\alpha = 0.97 \pm 0.11°$. Since the mean zenith angle θ_{med} for the Moon observations from the EAS-TOP array is $\theta_{med} = 31.5°$, σ_α has to be converted to the vertical: $\sigma_\alpha^{vert} = 0.83 \pm 0.1°$. The so obtained resolution includes systematic errors.

5.4. The zenith angle distribution

The EAS zenith angle (θ) distribution is shown in fig. 14 for internal events S_1. The best fit is provided by an $\exp(-n/\cos\theta)$ law (with $n = \gamma x_0/\lambda \approx 6.6$) up to $\theta \approx 65°$; for angles greater than 65° a deviation from this law (although not visible in the figure due to the scale) is seen, due to the contribution of horizontal air showers [19].

The resulting absorption mean free path of showers is $\lambda \approx 215$ g/cm^2, in agreement with the EAS measurements [13], and the barometric effect: $\beta = -(\Delta n/\Delta x)/n = 0.69\%$ mbar^{-1} ($\beta = \gamma/\lambda$, γ is the exponent of primary energy spectrum).

The difference in fitting the angular distribution with an exponential (solid line) or with a $\cos^n(\theta)$, $n = 8.4$, (dashed line) law shows that the shape is dominated by the physical effect of atmospheric absorption; distribution dominated by instrumental effects are best fitted with $\cos^n\theta$ behaviours.

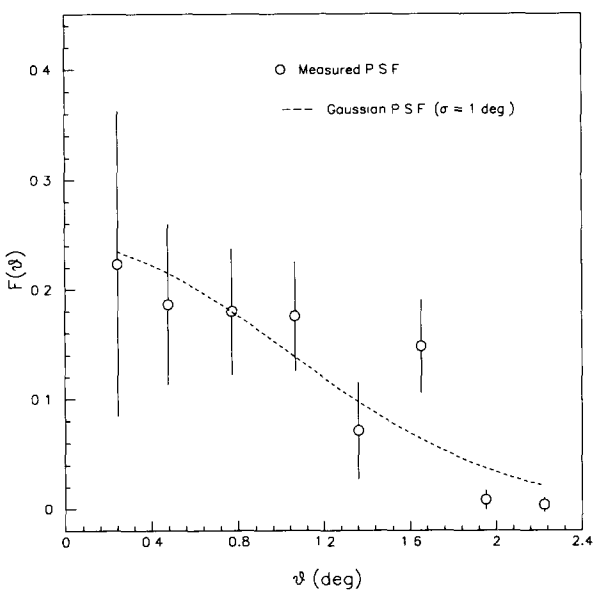

Fig. 13. Instrumental point spread function. The Gaussian point spread function for $\sigma = 1°$ is also shown (dotted line).

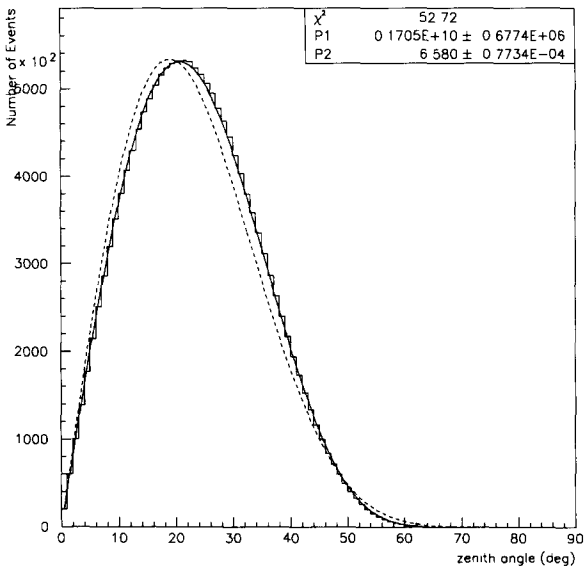

Fig. 14. Measured angular distribution in zenith angle for internal events. The "exponential" (solid line) and "$\cos^n\theta$" (dashed line) best fits are also shown.

5.5. An application: correlations with μ-detectors

The EAS-TOP e.m. array operates in coincidence with:

a) the GeV muon detector ($E_{\mu th} = 2$ GeV) operating at the surface (its angular resolution for single muons being $\sigma_\theta = 0.9°$). Comparing the arrival zenith angles of the showers as measured by the muon and e.m. detectors, the difference between the mean values is $\Delta\theta = 0.02° \pm 0.06°$, showing the absence of systematic relative effects at a level of 0.1° (90% c.l.);

b) the high energy (TeV) muon detectors located in the underground Gran Sasso laboratories (MACRO and LVD, whose muon energy threshold at the surface is $E_{\mu th} = 1.4$ TeV and for which the arrival directions are obtained by tracking systems, the angular uncertainties, mostly due to the muon scattering in the rock, being $\Delta\theta < 0.6°$ [7,8]). First coincidence events between EAS-TOP and the first supermodule of MACRO give for the mean values and widths of the two projections of the differences in arrival directions as measured by the two arrays: $\Delta\theta_x = 0.04° \pm 0.10°$ and $\Delta\theta_y = -0.20° \pm 0.12°$, and rms respectively $\sigma\theta_x = 1.0°$ and $\sigma\theta_y = 1.2°$ [7]. Within the statistics the mean values are compatible with the absence of systematic effects, and the rms of the distributions with both detectors resolutions.

6. Conclusions

The e.m. detector of EAS-TOP operates with an effective area $A_{eff} = 4 \times 10^4$ m^2 at $N_e > 2 \times 10^5$, i.e.

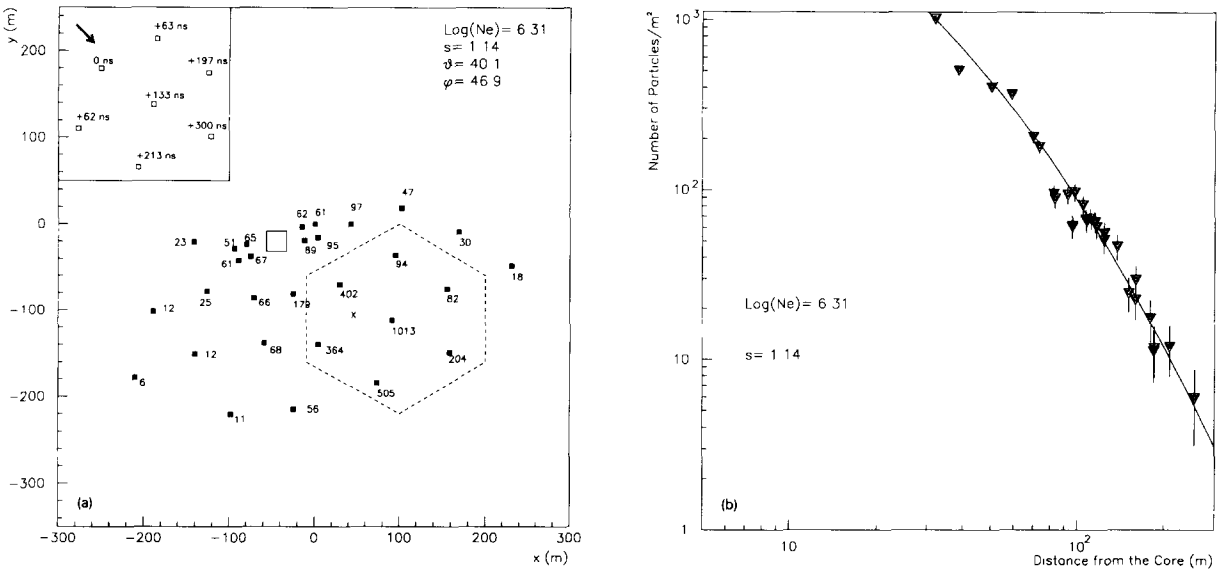

Fig. 15. (a) Full reconstruction of a UHE cosmic ray event: the particles number detected by each module is shown, together with the core position (indicated as a X), N_e, s, as reconstructed through the NKG fit, and the arrival direction as measured by the times of flight (see text). The modules used for the arrival direction determination are included within the dotted line their relative firing times (adjusted in order to take into account the different detectors heights and referred to the first fired one) are shown in the box in the upper part of the figure: the arrow indicates the event direction. (b) Experimental lateral distribution of the same event the solid line shows the best fit to the NKG formula.

mean proton primary energy $E_0 > 3 \times 10^{14}$ eV at the atmospheric depth $x = 810$ g/cm^2, and cosmic ray flux $\Phi = 3 \times 10^{-6}$ cm^{-2} s^{-1}sr^{-1}, the effective opening angle being $\Omega \approx 1$ sr. The reconstruction accuracies from the geometrical point of view allow good possibilities of combined analysis with other EAS detectors (tracking for muons and imaging for atmospheric Cherenkov light). From the energetic point of view the accuracy in the determination of N_e, $\sigma_{N_e}/N_e = 0.1$ is of the same order as the fluctuations in the shower size for protons of fixed primary energy ($E_0 \approx 10^{15}$ eV).

An example of a full reconstruction of a UHE cosmic ray event by the EAS-TOP array is shown in figs. 15a and 15b.

The detector is operating on different items of HE cosmic-ray physics for which the acceptance and the resolutions are of main importance, such as: the measurement of the primary spectrum [13], the study of the height of production of the different components (muons, atmospheric Cherenkov light [14]), the geometrical reconstruction and analysis of events observed in coincidence with the detectors operating in the underground Gran Sasso Laboratory [15,16], and the high angular resolution measurements in the field of UHE γ-ray astronomy [17,18].

Acknowledgements

The continuous cooperation of the Director and of the staff of the Gran Sasso Laboratories as well as the technical assistance of C. Barattia, R. Bertoni, M. Canonico, G. Giuliani, A. Giuliano and G. Pirali are gratefully acknowledged.

References

[1] M Aglietta et al (EAS-TOP Collaboration), Nuovo Cimento 9C (1986) 262.
[2] M. Aglietta et al. (EAS-TOP Collaboration), Nucl. Instr. and Meth. A 277 (1988) 23.
[3] M. Aglietta et al. (EAS-TOP Collaboration), Nuovo Cimento C 15 (1992) 735.
[4] M. Aglietta et al (EAS-TOP Collaboration), Studies of muons and of electromagnetic component of extensive air showers at EAS-TOP. Proc. 23rd ICRC, Calgary 19–30 July 1993, vol. 4, p 251
[5] M Aglietta et al. (EAS-TOP Collaboration) Nuovo Cimento C 15 (1992) 357;
Nuovo Cimento 105A (1992) 1807.

[6] C. Castagnoli et al., Proc. 22nd ICRC, Dublin, Ireland, 1991, vol. 4, p. 363.
[7] R. Bellotti et al. (MACRO and EAS-TOP Collaborations), Phys. Rev. D42 (1990) 1396
[8] M. Aglietta et al. (EAS-TOP and LVD Collaborations) Nuovo Cimento 105A (1992) 1815.
[9] G. Cocconi, Handbuch der Physik 46/1 (Springer, Berlin, 1961).
[10] F. James and M. Roos, MINUIT Function Minimization and Error Analysis, Release 89.12j, CERN Program Library D506 (1989).
[11] W.R. Nelson et al., The EGS4 Code System, SLAC-265 (1985).
[12] M. Aglietta et al. (EAS-TOP Collaboration) Proc 22nd ICRC, Dublin, Ireland, 1991, vol. 2, p. 708.
[13] M. Aglietta et al. (EAS-TOP Collaboration), The EAS primary spectrum between 10^{14} and 10^{16} eV (EAS-TOP data), Proc. 23rd ICRC, Calgary, 19–30 July 1993, vol. 4, p. 247.
[14] M. Aglietta et al. (EAS-TOP Collaboration), Study of EAS Cherenkov light images at EAS-TOP, Proc. of 23rd ICRC, Calgary, 19–30 July 1993, vol. 4, p. 700.
[15] EAS-TOP and MACRO Collaboration, Constraints on the PeV cosmic ray composition and interaction models from coincident EAS-TOP and MACRO data, Proc. 23rd ICRC, Calgary, 19–30 July 1993, vol. 2, p. 89.
[16] EAS-TOP and LVD Collaborations, Surface and deep underground observations of extensive air showers, Proc. 23rd ICRC, Calgary, 19–30 July 1993, vol. 4, p. 696.
[17] M. Aglietta et al. (EAS-TOP Collaboration), UHE γ-ray astronomy with the EAS-TOP array, Proc. 23rd ICRC, Calgary, 19–30 July 1993, in press.
[18] M. Aglietta et al. (EAS-TOP Collaboration) Astrophys. J. 397 (1992) 148.
[19] M. Aglietta et al. (EAS-TOP Collaboration), Study of horizontal air showers from EAS-TOP, Proc. 23rd ICRC, Calgary, 19–30 July 1993, vol. 4, p. 255.